Provided for non-commercial research and education use.
Not for reproduction, distribution or commercial use.

ISBN 978-94-007-5312-9

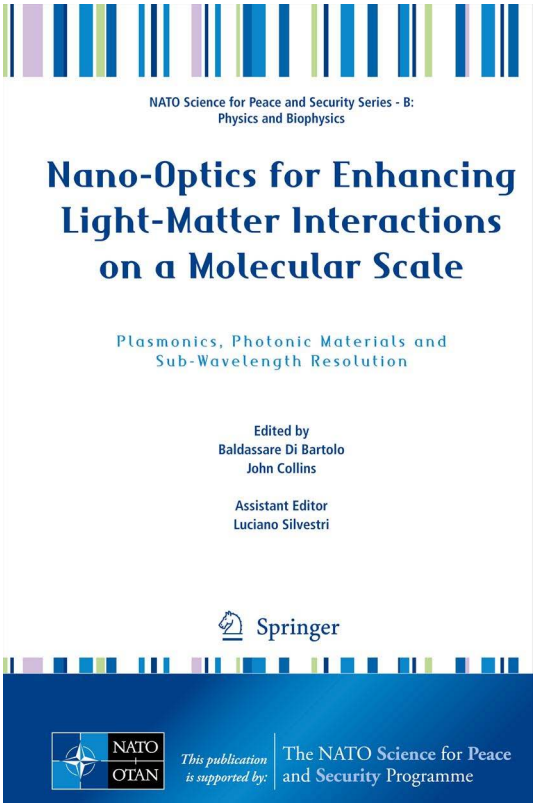

This chapter was published in the above Springer book. The attached copy is furnished to the author for non-commercial research and education use, including for instruction at the author's institution, sharing with colleagues and providing to institution administration.

Other uses, including reproduction and distribution, or selling or licensing copies, or posting to personal, institutional or third party websites are prohibited.

In most cases authors are permitted to post their version of the chapter (e.g. in Word or TEX form) to their personal website or institutional repository.

Author's personal copy

5
Raman Spectroscopy and Optical Coherence Tomography on a Micro-Chip: Arrayed-Waveguide-Grating-Based Optical Spectroscopy

Markus Pollnau, N. Ismail, B.I. Akca, K. Wörhoff, and R.M. De Ridder

Abstract We review our recent results on integrating biomedical optical systems onto a silicon chip.

5.1 Introduction

Miniaturization of optical instruments by integration onto an optical micro-chip will lead to smaller size and weight, reduction of optical coupling losses, avoidance of mechanical instabilities and the necessity for alignment, enormous cost reduction, and the potential for mass fabrication. Currently, individual waveguide components can be produced at the micrometer scale, such that total device footprints in the range of a few cm^2 can be obtained, but in the future individual device dimensions will scale down to the nanometer range by exploiting plasmonic waveguides, thereby allowing for complex optical systems to reach dimensions comparable to – and probably integrated with – electronic micro-chips.

In this chapter, we review our recent results on integrating optical systems for biomedical applications onto a silicon chip. Firstly, we investigated light collection from external samples by individual optical waveguides, showing that integrated waveguide probes can be more efficient than fiber probes when investigating thin samples. Then we extended this knowledge to confocal light delivery and collection by use of arrayed-waveguide gratings, thereby improving the light collection efficiency by an order of magnitude. Finally, we employed arrayed-waveguide gratings as integrated spectrometers in Raman spectroscopy and optical coherence tomography and demonstrated performance parameters that are well comparable to

M. Pollnau (✉) • N. Ismail • B.I. Akca • K. Wörhoff • R.M. De Ridder
Integrated Optical MicroSystems Group, MESA+ Institute for Nanotechnology, University of Twente, P.O. Box 217, Enschede, 7500 AE The Netherlands
e-mail: m.pollnau@ewi.utwente.nl

B. Di Bartolo et al. (eds.), *Nano-Optics for Enhancing Light-Matter Interactions on a Molecular Scale*, NATO Science for Peace and Security Series B: Physics and Biophysics, DOI 10.1007/978-94-007-5313-6_5,
© Springer Science+Business Media Dordrecht 2013

Author's personal copy

those of bulky and costly standard equipment. This achievement represents the first important step toward fully integrated biomedical optical instruments.

Our devices are fabricated in silicon oxynitride (SiON) technology. SiON is a promising material for integrated optical applications. Its refractive index can be chosen between the values of silicon dioxide (1.45) and silicon nitride (2.0), thus allowing for a flexible channel waveguide design [1]. A small bending radius of the channel waveguides down to several micrometers can be obtained by employing the highest refractive index contrast with an appropriate waveguide geometry. Furthermore, SiON is transparent in a broad wavelength range from 210 nm to beyond 2,000 nm [2], so that devices can be fabricated for both, the visible and infrared wavelength ranges by use of the same material system.

5.2 Efficiency of Integrated Waveguide Probes for the Detection of Backscattered Light

Numerous medical diagnostic methods are based on optical techniques such as Raman or fluorescence spectroscopy. One of the key challenges for their applicability is the realization of an efficient interface between the sample under investigation and the optical instrument, especially when a compact set-up is envisaged. Fiber-optic probes represent an excellent solution for *in-vivo* and *in-situ* measurements, if small dimensions and high flexibility of the probe are required [3], and fiber probes with different geometries have been extensively studied and characterized.

We explored the use of integrated optical waveguide probes as an alternative to fiber-optic probes. In particular, we compared their collection efficiency with those of large-core multi-mode and small-core single- and multi-mode fiber probes. For this purpose, we developed a semi-analytical model for integrated waveguide probes, under the condition that the sample is a weakly scattering medium [4]. For the case of highly scattering media, we performed Monte-Carlo simulations to understand quantitatively the collection of backscattered light by integrated waveguide probes [5].

We designed and fabricated an integrated waveguide probe having the geometry shown in Fig. 5.1. The probe has one excitation waveguide and eight collector waveguides with a silicon oxynitride (SiON) core and silicon oxide cladding. The propagation losses in SiON waveguides are approximately 0.4 dB/cm for the wavelengths of 532 and 693 nm used in our measurements [6]. The distance d between the waveguides is fixed to 11 μm, and each waveguide cross-section is 5×0.82 μm. The refractive indices of core and cladding at a wavelength of 532 nm have been estimated as 1.5321 (TE polarization) with a birefringence $\Delta n_{\mathrm{TM-TE}} = 2.1 \times 10^{-3}$, and 1.4631 (TE polarization) with a birefringence of 1×10^{-3}, respectively. The channels are equally spaced and all the collector waveguides are positioned on the same side with respect to the excitation waveguide. In this way it is possible to measure the backscattered light intensity as a function of lateral distance from the excitation point.

Author's personal copy

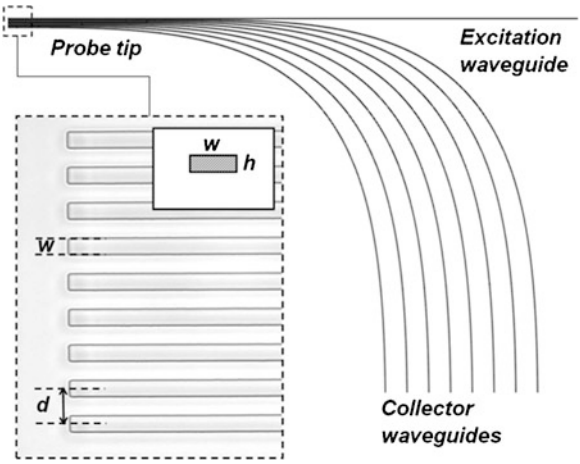

Fig. 5.1 Top view of a multi-waveguide silicon oxynitride (SiON) integrated probe for backscattered light collection. The *inset* shows an expanded view of the probe tip together with the waveguide cross-section, where $w = 5$ μm and $h = 0.82$ μm. The separation between adjacent waveguides is $d = 11$ μm (Figure taken from Ismail et al. [5])

Using the semi-analytical model, we compared our integrated waveguide probe and a similar probe with $d = 6$ μm with three different fiber probes: a typical Raman large-core multi-mode dual-fiber probe (core diameter of 200 μm) with $d = 210$ μm, a small-core multi-mode dual-fiber probe (core diameter of 5 μm) with $d = 11$ μm, and a small-core single-mode dual-fiber probe (core diameter of 3 μm) with $d = 11$ μm. For all fiber probes a refractive index contrast of 0.01 was assumed and the distance d between the excitation and collection channels was chosen such to prevent coupling of the waveguides through the evanescent tails of their modal fields. In all the simulations the excitation wavelength is 532 nm, while the wavelength of the collected signal is 693 nm.

Within the semi-analytical model we defined a figure of merit S, which is a measure of the collection efficiency of the different probes [4]. The results calculated for the different probes are shown in Fig. 5.2, in which the efficiency of each probe is displayed as a function of sample thickness. It becomes clear that, in case of thin samples (thicknesses t smaller than typically 110–150 μm), integrated waveguide probes provide efficiencies exceeding those of the investigated fiber probes. This result is relevant for various applications, e.g. Raman spectroscopy of the skin for determination of water content in the stratum corneum [7], which requires to detect the signal from regions within 100 μm underneath the sample surface. Furthermore, integrated probes have higher efficiency with respect to the investigated small-core fiber probes regardless of the sample thickness. Although it is not problematic to fabricate micro-fiber arrays with cores of, e.g., 5 μm diameter and similar distance apart from each other providing higher refractive index contrast than that investigated in our simulations, the advantages of integrated probes, such as reproducibility, low cost, and on-chip integration with other components, make them more suitable for applications that require probing of thin samples.

We carried out fluorescence measurements on a ruby rod [4]. The choice for ruby was made because the fluorescent signal in the red spectral region is very

Author's personal copy

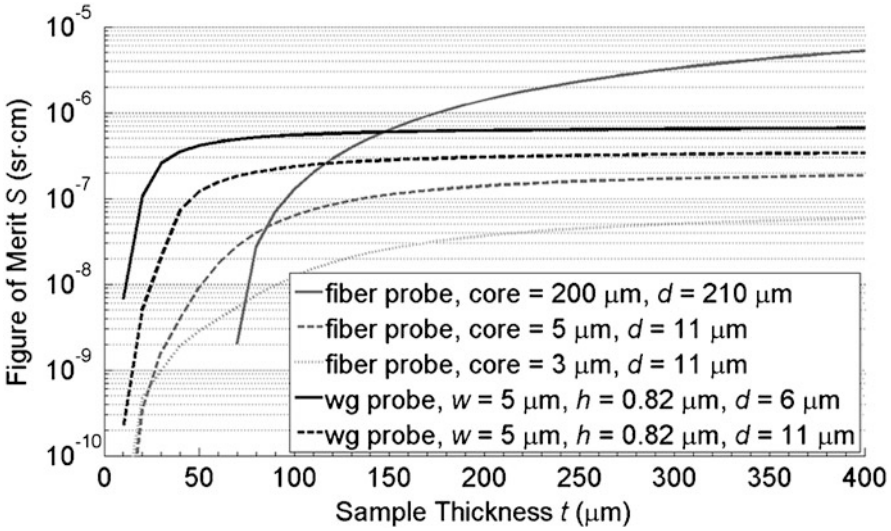

Fig. 5.2 Figure of merit S as a function of sample thickness t for two integrated dual-waveguide probes with cross-sections 5×0.82 μm and distances $d = 11$ μm and $d = 6$ μm (*black lines*), compared to those (*gray lines*) of a large-core dual-fiber probe with core diameter of 100 μm and $d = 210$ μm, and two small-core dual-fiber probes with $d = 11$ μm and core diameters of 5 and 3 μm, respectively (Figure taken from Ismail et al. [4])

strong and can easily be detected and distinguished from possible cross-talk of the excitation light. The measurements were performed using the integrated waveguide probe introduced in Fig. 5.1. Light from a Nd:YAG/SHG laser source at 532 nm was coupled into the excitation waveguide. With the ruby rod positioned in contact with the chip, fluorescence measurements were separately carried out on each of the eight collector waveguides. A small fraction of the fluorescence generated inside the ruby was captured by each of the eight collector waveguides. The comparison between the experimental results and the calculation performed with the semi-analytical model is shown in Fig. 5.3a. A second measurement was carried out by fixing d to 11 μm and measuring the power collected by the first collector waveguide of the probe at different distances of the ruby rod from the probe. The measurements compared to the simulation results are shown in Fig. 5.12b. In both, Fig. 5.12b, the comparison between measurements and simulations is achieved by normalizing each curve to its maximum value. The reasonable agreement between simulation and experiment validates our analytical model of integrated waveguide probes [4].

We also investigated excitation and light collection from a scattering medium by an integrated waveguide probe. Experiments were performed on light collection from a highly scattering water suspension of latex nanospheres. By use of the Monte-Carlo model, the propagation of light through the highly scattering medium was simulated and good agreement with the experimental data was found [5].

Author's personal copy

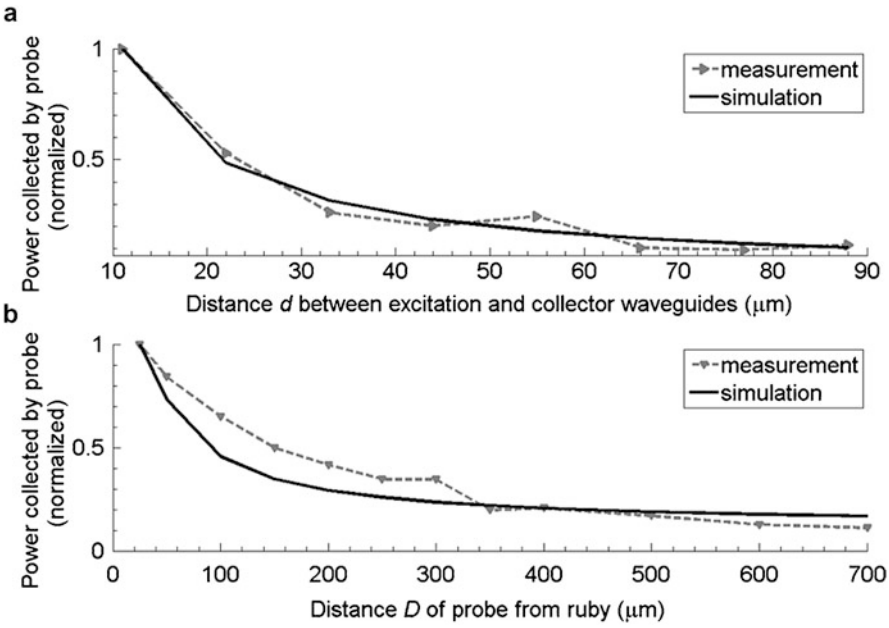

Fig. 5.3 (**a**) Fluorescence measured by a waveguide probe as a function of the distance d between excitation and collector waveguides; (**b**) Fluorescence measured by a dual-waveguide probe with $d = 11$ μm as a function of the distance D between the probe and the ruby (Figure taken from Ismail et al. [4])

5.3 Arrayed-Waveguide Gratings

The most important optical element for performing spectroscopy on a micro-chip is the integrated spectrometer. We have chosen to employ the arrayed-waveguide grating (AWG) [8]. Until now AWGs have been used for wavelength (de)multiplexing in telecommunication, offering high resolution over a small bandwidth [9]. Its working principle is schematically shown in Fig. 5.4a. Light from an input waveguide diverges in a first planar free propagation region (FPR) and illuminates the input facets of an array of channel waveguides. The channel waveguide array has a defined optical-path-length difference between adjacent channels. For a central wavelength λ_c, the phase difference at the output facets of adjacent array waveguides is an integer multiple of 2π. Since these facets are arranged on a circle, a cylindrical wavefront is formed at the beginning of a second FPR, which generates a focal spot at the central output channel. The phase shift caused by the length differences between arrayed waveguides is linearly dependent on wavelength, hence the resulting wavelength-dependent phase gradient implies a tilt of the cylindrical wavefront at the beginning of the second FPR. This causes the focal spot to shift with wavelength, i.e., different wavelengths are diffracted to different locations at the end of the FPR, at which either output channels or the pixels of a detector array can be positioned.

Author's personal copy

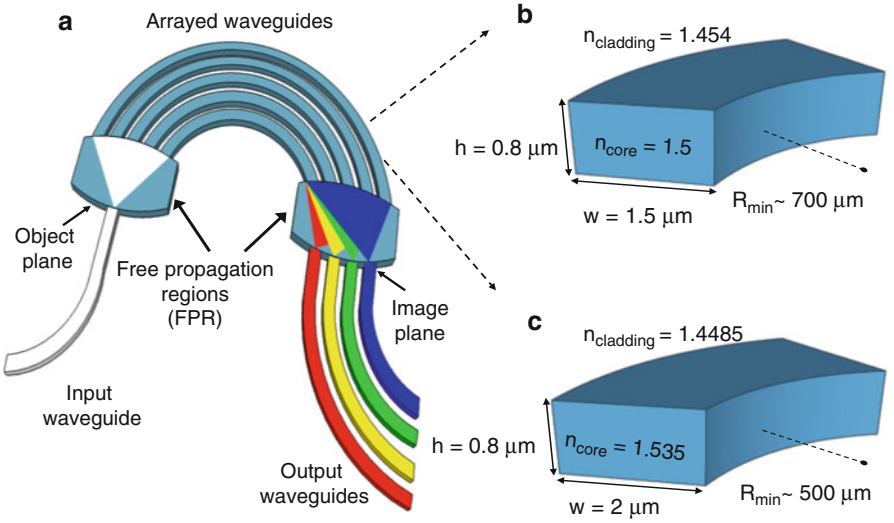

Fig. 5.4 (**a**) Schematic layout of an arrayed waveguide grating (AWG). Channel waveguide geometry for (**b**) an AWG with its central wavelength at 800 nm and (**c**) an AWG with its central wavelength at 1,300 nm (Figure taken from Akca et al. [10])

Compared to conventional spectrometers, the AWG has a small size ($\sim cm^2$) and can be integrated in a handheld device. Typical parameters of the individual waveguides for AWGs fabricated in SiON technology for the spectral ranges of 800 and 1,300 nm are displayed in Fig. 5.4c. A potential disadvantage of an AWG, the limited free spectral range (FSR) achievable for a given device size, can be overcome by a technology platform providing larger refractive index contrast, e.g. silicon photonics, or by accepting spectrally folded, yet non-overlapping peaks, as demonstrated in an example presented later in this chapter.

We described an improved AWG layout which applies identical bends across the entire array. In this way systematic phase errors arising from different bends that are inherent to conventional AWG designs are completely eliminated. In addition, for high-order AWGs our design resulted in more than 50% reduction of the occupied area on the wafer. A low-order device fabricated according to this geometry was experimentally characterized [11].

5.4 Confocal Light Delivery and Collection Using Arrayed-Waveguide Gratings

We invented a compact integrated optical device that combines the functions of light focusing, collection, and wavelength selection [12]. It makes use of two AWGs in a confocal arrangement. In its simplest design, displayed in Fig. 5.5, both AWGs

Author's personal copy

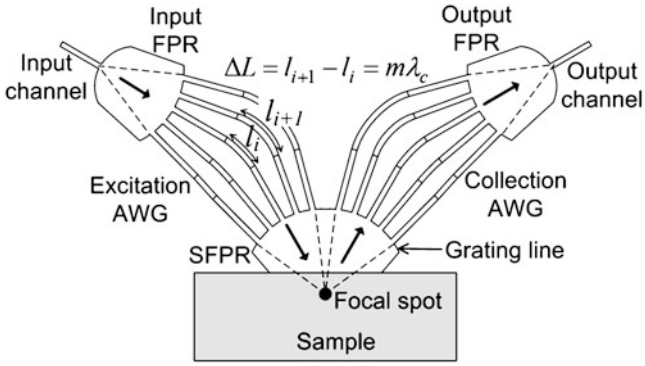

Fig. 5.5 Schematic of the confocal arrangement of two AWGs (with central wavelength λ_c and order m) which allows efficient illumination of, and signal collection from, a small focal volume below the sample surface (Figure taken from Ismail et al. [12])

have order $m = 0$, such that they form two lenses, the first one focusing a single excitation beam into the focal spot at a desired depth inside the sample and the second one collecting the light backscattered from this focal spot into a central output channel. In this arrangement the device behaves like a confocal microscope in one lateral direction. Enhanced functionality can be achieved without increasing device complexity by use of an AWG design exploiting the phase relation between the individual channels, thereby adding wavelength selectivity. As a result, the focusing AWG can have more than one input channel, allowing one to focus several excitation wavelengths into the same focal spot. Likewise, the collecting AWG can resolve different wavelengths emitted from the focal spot, thereby enabling spectral analysis of the backscattered light, if designed with the required wavelength spacing and FSR. In the particular case in which all excitation and signal wavelengths fall into the FSR of a single AWG, the same AWG can be used for both excitation and collection.

The focusing and collecting AWG are arranged in such a way that the output grating line – the interconnection line between the arrayed waveguides and the FPR – of the focusing AWG lies on the same circle and, hence, is concentric with the input grating line of the collecting AWG (Fig. 5.1). In this way the output FPR of the focusing AWG and the input FPR of the collecting AWG merge together, forming a single sample-side FPR. Ideally, its length is chosen such that when in contact with a sample the focal spot is located at the desired depth d below the sample surface (for a given sample refractive index n_S) in order to allow for maximum collection efficiency in the direction perpendicular to the device plane.

In our investigations, we focused on demonstrating that our approach improves the collection efficiency of signal light by more than an order of magnitude compared to standard light collection using a single-mode waveguide. Two similar AWGs were compared. The "reference" AWG is of a conventional design, having a single monomodal input channel for light collection and an AWG for spectral

Author's personal copy

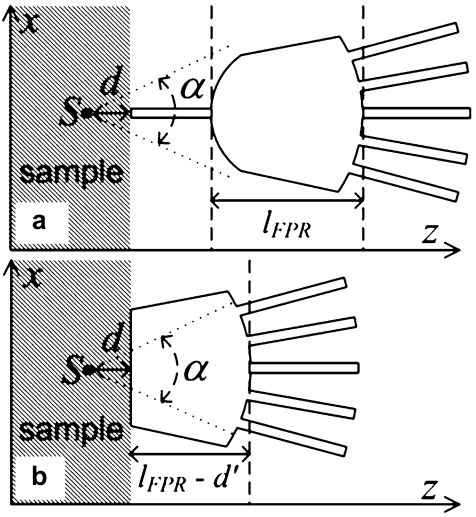

Fig. 5.6 Input sections of (**a**) a "reference" (standard) AWG and (**b**) a "collector" AWG (the proposed device), both positioned at a distance d from a source S (Figure taken from Ismail et al. [12])

analysis with an input FPR of length l_{FPR}, see Fig. 5.6a. In contrast, the "collector" AWG is of the proposed design; see Fig. 5.6b. Its input FPR is shortened to a length $l_{SFPR} = l_{FPR} - d'$, where d' depends on the distance d of the input facet to the source (if n_S is equal to the effective index of the sample-side FPR, then $d' = d$).

As a source of signal light at point S we used light at a wavelength of 1284.6 nm emitted from either a standard 9-μm fiber with an angular aperture of $\alpha = 9.2°$ or an ultra-high-numerical-aperture fiber with $\alpha = 29°$, with air (refractive index $n_d = 1$) between source and device. Subsequently, index-matching liquid was placed between each fiber and the chip to reduce the angular aperture to $\alpha = 5.7°$ and 19.6°, respectively. The fiber output end was positioned at variable distance d from the chip. Firstly, we performed measurements with the reference AWG for all four α at varying distance d. Secondly, measurements were performed on the repeatedly diced collector AWG at four distances $d = 50$, 100, 150, and 200 μm. The collector AWG was measured only with index-matching liquid ($\alpha = 5.7°$ and 19.6°) to average out the roughness of the diced facet. The measured output power of reference and collector AWG is shown in Fig. 5.7b, respectively, as a function of d. Furthermore, the collection efficiency of both devices was calculated as a function of d. Experiments and calculations show that, as d increases, all curves exhibit a monotonous decay which is steeper for the reference compared to the collector AWG, because light collection by the former is limited in both, horizontal and vertical directions by the cross-section of the input channel, while for the latter this limitation occurs only in the vertical direction. This difference results in higher collection efficiency of the collector AWG compared to the reference AWG. Finally, also multi-wavelength imaging was demonstrated utilizing this device [12].

Author's personal copy

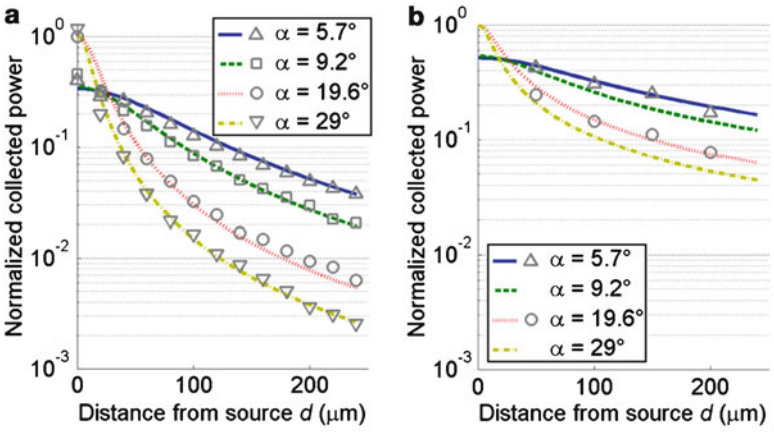

Fig. 5.7 Comparison of measured (*symbols*) and calculated (*lines*) power collected by (**a**) the reference AWG and (**b**) the collector AWG, normalized to the power collected by the reference AWG at $d = 0$ and $\alpha = 19.6°$, versus source-to-input facet distance d for different values of the source angular aperture α (Figure taken from Ismail et al. [12])

5.5 Integrated Raman Spectroscopy with an Arrayed-Waveguide Grating

In numerous applications, Raman spectroscopy is utilized to monitor unique ("fingerprint") Raman scattering in order to identify specific molecules or structures. We aimed at developing a low-cost, compact, hand-held apparatus for polarized Raman spectroscopy, specifically for the detection of dental caries at an early state [13]. A critical function of such a system is spectral separation of the Raman-scattered signals. In our case, the core element of such a device is an AWG.

We chose an excitation wavelength of $\lambda_0 = 830$ nm and designed the wavelength-selective AWG to have a central wavelength of $\lambda_c = 901$ nm and a FSR of $\sim$22 nm between 890 and 912 nm, with a resolution of 0.2 nm. The center-to-center spacing between the 271 arrayed waveguides at the FPR interface was 6 μm, and so was the spacing between the output channels of the AWG. From these parameters it is possible to calculate the dispersion angle of the AWG from well established equations [9], and determine the length R of the FPR (see inset to Fig. 5.8), which results in approximately 4 mm. The AWG layout was drawn by imposing a minimum bending radius of 1,700 μm to guarantee bending losses below 0.1 dB/cm when taking into account fabrication tolerances.

The setup used in the Raman experiments is shown in Fig. 5.1. Light from a linearly polarized, tunable Ti:Sapphire laser at 830 nm is sent through a polarization beam splitter (PBS) oriented parallel to the laser polarization. A half-wave plate is

Author's personal copy

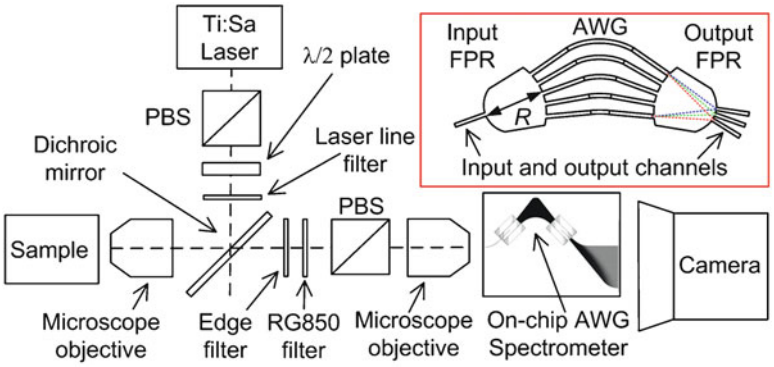

Fig. 5.8 Setup used for the polarized Raman experiments. *Inset*: schematic of arrayed waveguide grating (AWG) (Figure taken from Ismail et al. [14])

positioned after the PBS, initially with one of its optical axes parallel to the laser polarization, so that the polarization is not rotated. The laser light exiting the λ/2 plate, after passing through a laser-line filter, is reflected from a dichroic mirror and focused onto the sample with a microscope objective. The light backscattered from the sample is then collected by the same optics. The Rayleigh-scattered component is again reflected (rejected) by the dichroic mirror, which transmits the Raman-scattered wavelengths. An edge filter and an additional red-glass filter are used to further suppress residual reflected and Rayleigh-scattered light at the laser wavelength, that entering the AWG would be imaged at a higher order on the lateral output channels. At this point the light passes through another PBS with the same orientation as the first PBS, and is focused onto the input channel of the integrated AWG spectrometer by a microscope objective. The output channels of the AWG are imaged onto an electron-multiplying charge-coupled device (EMCCD) through a camera lens. In order to perform the measurements for perpendicular polarization, we rotate the λ/2 plate by ∼45°, so that the polarization of the excitation laser is rotated by 90°. In both, parallel and cross-polarization measurements light entering the AWG is always horizontally polarized (TE polarization with respect to the input waveguide).

We performed Raman measurements on cyclohexane [14]. The inset of Fig. 5.9 displays the unpolarized Raman spectrum of cyclohexane in the fingerprint region (400–1,600 cm^{-1}), as measured using a bulk Raman spectrometer (based on a Model 2,500 High Performance Raman Module, River Diagnostics B.V.). With the excitation wavelength of 830 nm, the Raman signals of cyclohexane occur in the wavelength range between 859 and 957 nm. Since this wavelength range exceeds almost fivefold the FSR of 22 nm (at the central wavelength λ_c) of our AWG, the different parts of the Raman spectrum fall into five different diffraction orders ($m = 39, 40, 41, 42$, and 43) of the AWG, as indicated in the inset.

Author's personal copy

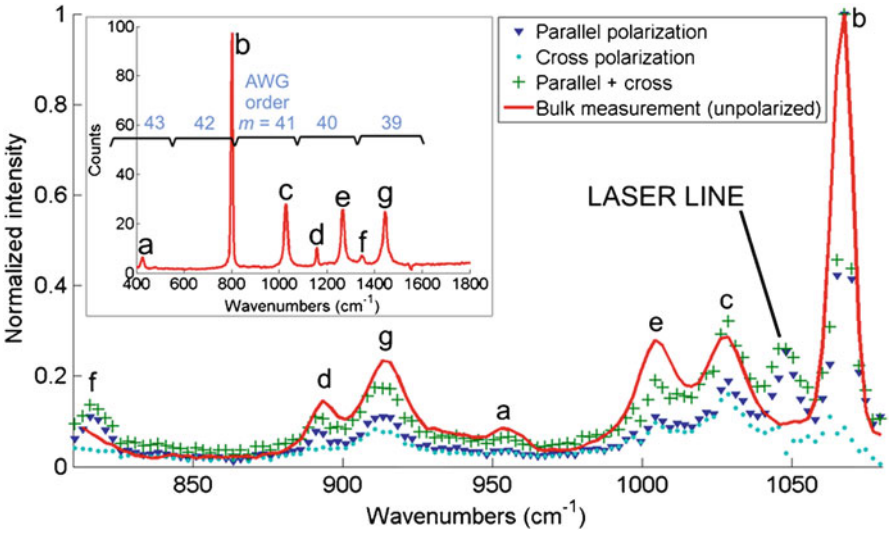

Fig. 5.9 Normalized Raman spectra of cyclohexane for parallel (*triangles*) and cross (*dots*) polarization, measured with the AWG spectrometer; normalized sum of the two spectra (*crosses*). Unpolarized Raman spectrum (*solid line*) measured with a conventional spectrometer, folded into diffraction order $m = 41$ of the AWG. *Inset*: original unfolded spectrum, extending over diffraction orders $m = 39$, 40, 41, 42, and 43 of the AWG. The individual Raman peaks in both, folded and unfolded spectrum, are assigned by letters (*a–g*). An additional peak at 1,050 cm^{-1} is attributed to the laser line imaged at a higher order ($m = 45$) (Figure taken from Ismail et al. [14])

The same Raman spectrum, with the different diffraction orders folded into the diffraction order $m_{AWG} = 41$, for which the AWG was designed, is calculated with the AWG grating equation [15] and shown as a red line in Fig. 5.9. The individual peaks in the original and folded spectrum are assigned by letters (a–g). Using our AWG spectrometer, polarized Raman signals were measured. Figure 5.9 shows the signals measured for parallel (triangles) and cross (dots) polarization, normalized to the intensity of peak b for parallel polarization. Comparison of the normalized sum of these two signals (green crosses) with the unpolarized spectrum (red line) of cyclohexane, as measured using the bulk spectrometer and folded into the diffraction order of the AWG, shows very good qualitative agreement: first of all, we observe the presence of strongly polarized Raman bands at the locations of peaks b and d, in agreement with the results found in the literature [16]. Furthermore, all the peaks of cyclohexane in the fingerprint region can be clearly distinguished. This test result demonstrates that a measurement with an AWG spectrometer can unambiguously identify the Raman fingerprint of a measurand, even if its Raman spectrum exceeds the FSR of the AWG, thus allowing us to design and apply an AWG with high spectral resolution. Furthermore, polarized Raman spectra were measured of extracted human teeth containing localized initial carious lesions [14].

Author's personal copy

5.6 Integrated Optical Coherence Tomography with an Arrayed-Waveguide Grating

Optical coherence tomography (OCT) [17] is a non-invasive optical technique for high-resolution cross-sectional imaging of biological tissue, with many applications in clinical medicine. The measurement principle of OCT is based on low-coherence interferometry (LCI) in which interference patterns due to the superposition of a multitude of waves with a large spread in wavelengths are studied. These distinctive patterns enable one to determine the location at which light is reflected back and to measure the depth profile of the scattering amplitude. By performing multiple LCI measurements at different lateral coordinates on a sample, a three-dimensional cross-sectional image of the scattering amplitude can be constructed.

Current state-of-the-art OCT systems operate in the Fourier-domain [18], using either a broad-band light source and a spectrometer, known as spectral-domain OCT (SD-OCT), or a rapidly tunable laser, known as swept-source OCT (SS-OCT), because they offer a significant sensitivity advantage over time-domain OCT. SD-OCT systems can utilize simple broadband sources, however they suffer from severe signal roll-off in depth and require complicated detection optics, i.e., linescan cameras and spectrometers. Current commercial SD-OCT systems typically achieve $\sim$5 μm axial resolution with $\sim$25–27 kHz axial scan rates over an imaging range of $\sim$2.0–2.6 mm. OCT systems contain a multitude of fiber and free-space optical components which make these instruments costly and bulky. The size and cost of an OCT system can be decreased significantly by the use of integrated optics. In addition, integrated optics can enhance the performance of OCT by, for example, parallelization [19, 20] of OCT devices on a chip.

A key component of an SD-OCT system is the high-resolution spectrometer. We employ the same type of AWG that we successfully used in Raman spectroscopy (Sect. 5.5). We investigated AWG spectrometers with high resolution and large FSR for the spectral ranges near 800 and 1,300 nm in interferometric depth ranging and OCT imaging, thereby demonstrating the first important step toward miniaturization of an SD-OCT system.

The essential parameters that determine the imaging quality of FD-OCT systems are center wavelength, axial resolution, maximum imaging depth, signal-to-noise ratio (SNR), and sensitivity roll-off in depth. The shorter center wavelength of 800 nm is used for imaging ophthalmic structures to avoid the water absorption losses dominant in this application, whereas for dermal imaging 1,300 nm is used to avoid the dominant scattering losses. The axial resolution of an SD-OCT system is determined by the effective bandwidth of the detected light, which depends on the bandwidth of the light source and the FSR of the spectrometer. Matching the FSR of the AWG with the bandwidth of the light source is the most economical configuration. The maximum imaging depth in SD-OCT is determined by the spectral sampling interval. The imaging range of SD-OCT is limited by the signal roll-off, which is the attenuation of the OCT signal due to washout of the interference fringe visibility with increasing depth. The roll-off in depth of

Author's personal copy

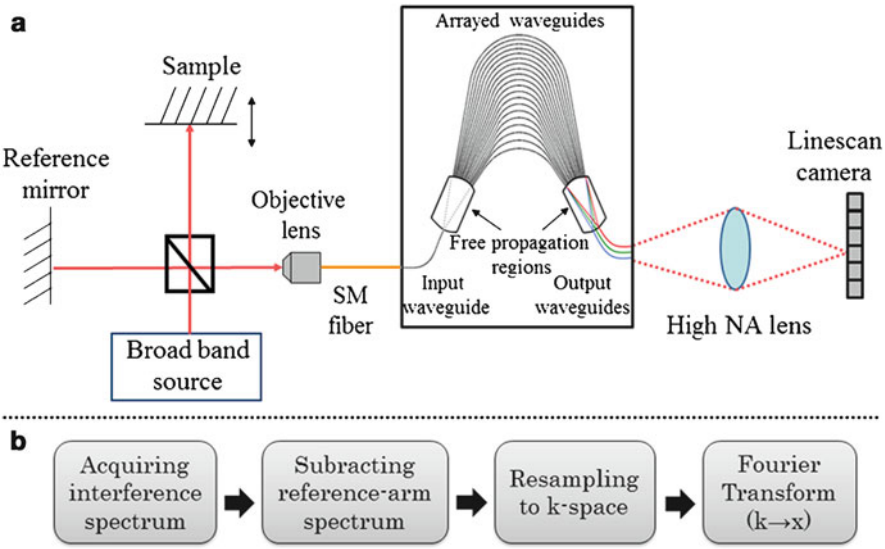

Fig. 5.10 (**a**) Optical measurement set-up of the SD-OCT system with free-space Michelson interferometer and integrated AWG spectrometer; (**b**) signal processing steps for SD-OCT (Figure taken from Akca et al. [10])

the SD-OCT signal is determined by the spectral content of the spectrometer and the camera pixel size. Finally, for maximum SNR, the spectrometer loss should be minimized in the design stage. Typical SNR values for high-quality OCT imaging are on the order of 100 dB. For more details, see [10].

A schematic of the SD-OCT system with integrated AWG spectrometer is shown in Fig. 5.10a. The measurement technique for the 800 and 1,300 nm spectral ranges is similar, except for the different specifications of the light source and the linescan camera. The free-space Michelson interferometer (MI) is illuminated with a superluminescent diode emitting a Gaussian-like spectrum. Light from the source is directed to the reference and sample arms by a 50:50 beam splitter. The reference mirror is kept stationary, while the sample mirror is moved during the experiments. Light returning from the two arms is focused by an objective lens into a single-mode fiber and directed to the AWG spectrometer. The output power of the MI is measured to be 0.1 and 0.9 mW for the 800 and 1,300 nm spectral ranges, respectively. In the AWG spectrometer, the optical spectrum is dispersed by the arrayed waveguides and imaged by a camera lens with high numerical aperture onto the camera. The acquired spectra are processed by subtracting the reference-arm spectrum and resampling to k-space, as indicated in Fig. 5.10b. The reflectivity depth profile is obtained by performing a Fourier transformation of the digitized camera output. The measured spectra have an absolute wavelength scale defined by the center wavelength and FSR value of the AWG.

The spectrum shown in Fig. 5.11a is the spectrum from the reference arm at 1,300 nm. The optical bandwidth of the spectrum is measured as 39 nm.

Author's personal copy

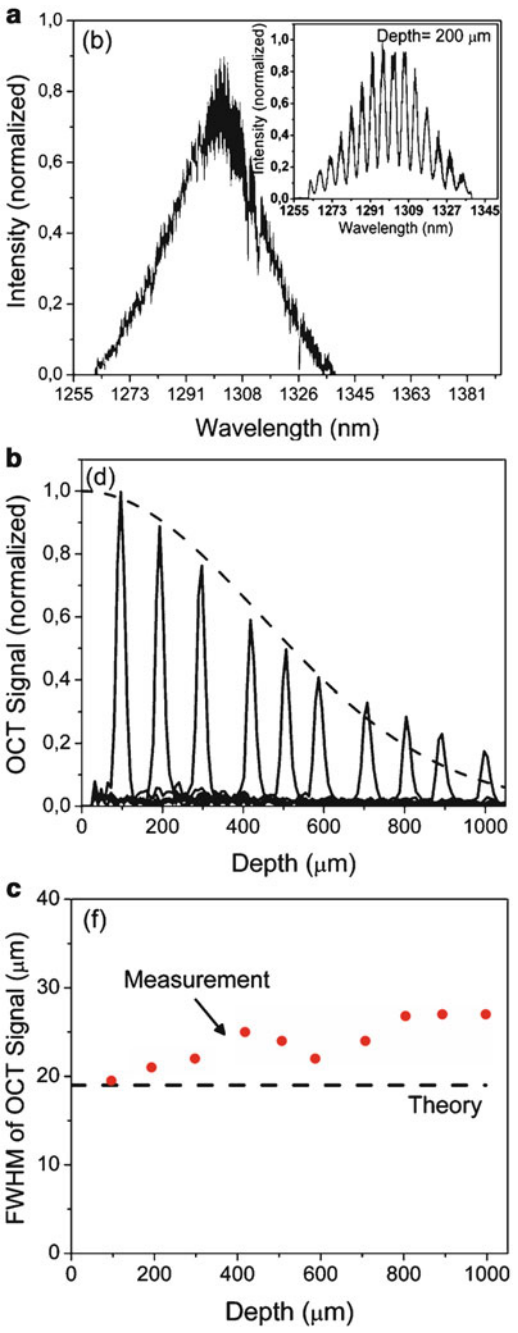

Fig. 5.11 Measured data for an 1,300-nm AWG: (**a**) Reference spectrum of the AWG spectrometer on the linescan camera. The *inset* shows the interference spectrum measured at 200 μm depth after background subtraction. (**b**) OCT signal as a function of depth for a mirror reflector and fit of the roll-off (*dashed line*). The maximum depth range is 1 mm. (**c**) OCT axial resolution (*solid circles*) in comparison with the theoretical axial resolution (*dashed line*) (Figure taken from Akca et al. [10])

Author's personal copy

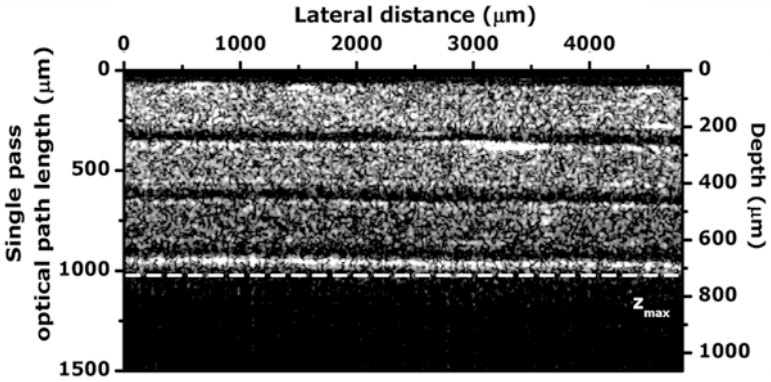

Fig. 5.12 OCT image of a three-layered scattering phantom measured with the AWG as spectrometer in SD-OCT. The *dashed line* indicates the maximum imaging depth (Figure taken from Nguyen et al. [22])

This value corresponds to an axial resolution of 19 μm. The inset shows the measured interference spectrum after background subtraction, measured at a depth of 200 μm. The modulation on the spectrum due to interference can be clearly observed. The OCT signals measured for different depths, i.e. for different path length differences between sample and reference arm of the MI, are shown in Fig. 5.11b. The depth scale corresponded one-to-one with the physical distance of the sample arm position change. We achieved imaging up to the maximum depth range of 1 mm. The measured signal-to-noise ratio (SNR) was 75 dB at 100 μm depth, which includes 10 dB fiber-to-chip coupling loss, 7 dB free-space interferometer loss, and 5 dB chip-to-camera coupling losses. By reducing losses and increasing the output power of the light source, the sensitivity of the SD-OCT system using an AWG spectrometer can be improved to the level of state-of-the-art OCT systems. The FWHM values of the point spread functions at various depths are plotted in Fig. 5.11c. An experimental axial resolution of 20 μm at 100 μm depth was obtained. A decrease in resolution was found at larger depths.

As a demonstration of OCT cross-sectional imaging using the AWG spectrometer, an image of a three-layered scattering phantom was obtained when using part of a fiber-based OCT set-up [21] with the AWG as spectrometer, see Fig. 5.12 [22]. As expected, all three scattering layers are observed up to the maximum single-pass optical path length of 1 mm (725 μm depth for the average refractive index of 1.38 of the phantom). The current imaging resolution and depth are sufficient for biological imaging but can be improved by increasing the FSR and the number of output channels.

Finally, the effect of discrete output channels and polarization dependency of an AWG spectrometer was investigated [23]. By removing the output waveguides of the AWG, the depth range was enhanced from 1 to 3.3 mm. In addition, the effect of polarization dependency of the AWG on sensitivity roll-off was investigated and, for

Author's personal copy

partial polarization, a beat effect was observed in the depth ranging measurements, which leads to signal fading at specific depths. By controlling the polarization state of the light carefully, the signal fading could be eliminated. A polarization-independent AWG was investigated, which eliminated without the use of extra components for polarization control.

5.7 Conclusions

Exploiting the spectral properties of AWGs, we have demonstrated confocal light delivery and collection as well as Raman spectroscopy and SD-OCT with the spectrometer integrated on a silicon chip. Integration of additional optical components onto the same micro-chip will enable low-cost mass fabrication of integrated optical instruments for various applications. Considerable size reduction of the optical structures, e.g. by exploiting plasmonic structures, could provide sufficient compatibility in lithography and processing for the combination of optical with electronic functions, e.g. signal processing, on the same chip.

Acknowledgments The authors thank A. Driessen for many fruitful discussions, A. Hollink, G. Sengo, and M. Dijkstra for technical assistance, as well as V. D. Nguyen, J. Kalkman, and T. G. van Leeuwen from the Academic Medical Center, University of Amsterdam, The Netherlands, A. C. Baclig, P. J. Caspers, and G. J. Puppels from the Erasmus-University Medical Center Rotterdam, The Netherlands, and L. P. Choo-Smith from the National Research Council Canada, Winnipeg, Manitoba, Canada for their contributions to the experiments. This work was supported within the Innovative Research Program (IOP) Photonic Devices funded by the Dutch Ministry of Economic Affairs and the Dutch Senter-Novem MEMPHIS Project.

References

1. Wörhoff K, Roeloffzen CGH, de Ridder RM, Driessen A, Lambeck PV (2007) Design and application of compact and highly tolerant polarization-independent waveguides. IEEE J Lightwave Technol 25:1276–1282
2. Wörhoff K, Klein EJ, Hussein MG, Driessen A (2008) Silicon oxynitride based photonics. In: Proceedings of the international conference on transparent optical networks, Athens, Greece, pp 266–269
3. Utzinger U, Richards-Kortum RR (2003) Fiber optic probes for biomedical optical spectroscopy. J Biomed Opt 8:121–147
4. Ismail N, Civitci F, Wörhoff K, de Ridder RM, Pollnau M, Driessen A (2011) Efficiency of integrated waveguide probes for the detection of light backscattered from weakly scattering media. Appl Opt 50:935–942
5. Ismail N, Sun F, Wörhoff K, Driessen A, de Ridder RM, Pollnau M (2011) Excitation and light collection from highly scattering media with integrated waveguides. IEEE Photon Technol Lett 23:278–280
6. Wörhoff K, Hilderink LTH, Driessen A, Lambeck PV (2002) Silicon oxynitride: a versatile material for integrated optics applications. J Electrochem Soc 149:85–91

Author's personal copy

7. Caspers PJ, Lucassen GW, Carter EA, Bruining HA, Puppels GJ (2001) In vivo confocal Raman microspectroscopy of the skin: noninvasive determination of the molecular concentration profiles. J Invest Dermatol 116:434–442
8. Smit MK (1988) New focusing and dispersive planar component based on an optical phased array. Electron Lett 24:87–88
9. Smit MK, van Dam C (1996) PHASAR-based WDM-devices: principles, design and applications. J Sel Top Quantum Electron 2:236–250
10. Akca BI, Nguyen VD, Kalkman J, Ismail N, Sengo G, Sun F, Driessen A, van Leeuwen TG, Pollnau M, Wörhoff K, de Ridder RM (2012) Toward spectral-domain optical coherence tomography on a chip. IEEE J Sel Top Quantum Electron 18:1223–1233
11. Ismail N, Sun F, Sengo G, Wörhoff K, Driessen A, de Ridder RM, Pollnau M (2011) Improved arrayed-waveguide-grating layout avoiding systematic phase errors. Opt Express 19:8781–8794
12. Ismail N, Akca BI, Sun F, Wörhoff K, de Ridder RM, Pollnau M, Driessen A (2010) Integrated approach to laser delivery and confocal signal detection. Opt Lett 35:2741–2743
13. Ko CT, Choo-Smith LP, Hewko M, Sowa MG, Dong CCS, Cleghorn B (2006) Detection of early dental caries using polarized Raman spectroscopy. Opt Express 14:203–215
14. Ismail N, Choo-Smith LP, Wörhoff K, Driessen A, Baclig AC, Caspers PJ, Puppels GJ, de Ridder RM, Pollnau M (2011) Raman spectroscopy with an integrated arrayed-waveguide grating. Opt Lett 36:4629–4631
15. Takahashi H, Oda K, Toba H, Inoue Y (1995) Transmission characteristics of arrayed waveguide $N \times N$ wavelength multiplexer. J Lightwave Technol 13:447–455
16. Pelletier MJ (1999) Effects of temperature on cyclohexane Raman bands. Appl Spectrosc 53:1087–1096
17. Huang D, Swanson EA, Lin CP, Schuman JS, Stinson WG, Chang W, Hee MR, Flotte T, Gregory K, Puliafito CA, Fugimioto JG (1991) Optical coherence tomography. Science 254:1178–1881
18. Fercher AF, Hitzenberger CK, Kamp G, Elzaiat SY (1995) Measurement of intraocular distances by backscattering spectral interferometry. Opt Commun 117:3–48
19. Bourquin S, Seitz P, Salathé RP (2001) Optical coherence tomography based on a two-dimensional smart detector array. Opt Lett 26:512–514
20. Bourquin S, Laversenne L, Rivier S, Lasser T, Salathé RP, Pollnau M, Grivas C, Shepherd DP, Eason RW (2005) Parallel broadband fluorescent light source for optical coherence tomography. In: Proceedings of the SPIE, coherence domain optical methods and optical coherence tomography in biomedicine IX, vol 5690. San Jose, CA, USA, pp 209–213
21. Kalkman J, Bykov AV, Faber DJ, van Leeuwen TG (2010) Multiple and dependent scattering effects in Doppler optical coherence tomography. Opt Express 18:3883–3892
22. Nguyen VD, Akca BI, Wörhoff K, de Ridder RM, Pollnau M, van Leeuwen TG, Kalkman J (2011) Spectral domain optical coherence tomography imaging with an integrated optics spectrometer. Opt Lett 36:1293–1295
23. Akca BI, Chang L, Sengo G, Wörhoff K, de Ridder RM, Pollnau M (2011) Performance improvement of spectral-domain optical low-coherence reflectometry using an arrayed-waveguide grating, submitted